Materials & Design 262 (2026) 115448

Contents lists available at ScienceDirect

Materials & Design

journal homepage: www.elsevier.com/locate/matdes

Tuning surface microtopography for optimum thermocompression bonding performance: structure, process parameters, and mechanisms on microfluidic chips

Baishun Zhao [a,b], Dimitrios Kontziampasis [c], Zhiyu Yang [d], Bingyan Jiang [b], Wangqing Wu (吴旺青) [b,*], Dou Zhang [a,*]

[a] State Key Laboratory of Powder Metallurgy, Powder Metallurgy Research Institute, Central South University, Changsha 410083, China
[b] State Key Laboratory of Precision Manufacturing for Extreme Service Performance, School of Mechanical and Electrical Engineering, Central South University, Changsha 410083, China
[c] Institute of Medical and Biological Engineering, School of Mechanical Engineering, Faculty of Science and Engineering, University of Leeds LS2 9JT Leeds, Yorkshire, UK
[d] Jingmu (Zhuhai) Company Limited, Zhuhai 519055 Guangdong, China

ARTICLE INFO

Keywords:
Microfluidics
Simulation
Thermal bonding
Polymer
Microfabrication

ABSTRACT

The widespread application of microfluidic chips in biomedicine, life sciences, and food safety has generated industrialization demands, making it necessary to address key challenges in production costs and scalability. This work proposes the fabrication of an innovative microstructure in microfluidic chips to enhance thermocompression bonding performance. Through simulation, the stress mitigation effect of the energy-gathering rib (ER) and the resulting microchannel deformation are analyzed. This analysis subsequently feeds a redesign of the initial reference microchannel structure, acting as a guide. Experimental validation follows to confirm the enhancement of bonding performance by the ER. Results demonstrate that compared to the initial microchannel, the new design increases bonding strength by 123 % and reduces microchannel deformation by 6–8.46 %. Further analysis reveals that bonding strength increases by 160 % in the pressure range of 0.6–1.56 MPa. Additionally, this work advances the general understanding of the bonding strength formation mechanism by clearly elucidating the evolutionary behavior of interfacial morphology at the bonded interface. The generated knowledge accelerates the commercialization of microfluidic chips by directly improving the economic efficiency and sustainability of the fabrication process.

1. Introduction

Microfluidic chips consist of channels ranging from the micron to millimeter scale and offer high automation and throughput, low cost, and compact size [1,2]. These devices are typically fabricated for the control and manipulation of fluids [3], droplets [4], mixtures [5], or liquid solutions of biological matter (i.e. proteins, cells, bacteria) [6]. Microfluidic chips are directly connected with the development and progression of important fields [7], including biomedical diagnostics [8], drug screening [9], environmental monitoring [7,10], and food safety [11,12]. One of the main focuses in microfluidic chip development currently revolves around cost reduction. Simultaneously, to meet the requirements posed by these fields, scale-up is necessary to achieve commercialization [13].

Bonding technology is one of the key processes during batch manufacturing of microfluidic chips, its quality and efficiency directly affect device performance, production cost, and manufacturing efficiency [14,15]. Numerous bonding methods have been proposed for the fabrication of microfluidic chips, i.e. ultrasonic bonding [16], thermal-assisted ultrasonic bonding [17], solvent bonding [18,19], plasma bonding [20], and media-assisted bonding [21]. Nevertheless, thermocompression bonding offers a unique combination of advantages that include simplicity, ease of implementation, and the avoidance of secondary pollution [3,15]. Specifically, this method does not require the use of volatile organic compounds (VOCs) or solvents, which are commonly associated with solvent-based bonding techniques [22,23]. Additionally, compared to ultrasonic or laser welding, thermocompression bonding does not require specialized (ultrasonic or laser)

* Corresponding authors.
E-mail addresses: csuwwq@csu.edu.cn (W. Wu (吴旺青)), dzhang@csu.edu.cn (D. Zhang).

https://doi.org/10.1016/j.matdes.2026.115448
Received 15 October 2025; Received in revised form 15 December 2025; Accepted 4 January 2026
Available online 5 January 2026

equipment [24]. However, this method typically achieves low bonding strength, occasionally leads to significant shrinkage and deformation of microchannels, which hinder its advancement and widespread adoption.

In the current literature, efforts focus on refining the thermocompression bonding process to improve bonding quality and fabrication efficiency. The most notable approaches include bonding parameter optimization, surface treatments, and bonding tool design. One approach integrates thermocompression bonding technology into a microfluidic chip injection mold [25]. This method, also referred to as in-mold thermocompression bonding, effectively combines the benefits of injection molding with those of thermocompression bonding to promote the commercialization of microfluidic chips. Other researchers propose a dynamic tempered in-mold thermocompression bonding technique aimed at improving production efficiency for microfluidic chips. Results validate that this approach demonstrates optimal bonding process characteristics and quality, as evaluated through the variability of different bonding indicators in response to different experimental factors [26,27]. Another approach uses an orthogonal experiment to assess the impact of process factors on the height of triangular channels, using height deformation as an evaluation criterion. Their conclusions contradict those of others in the literature [26], as they claim that the significant factors impacting microchannel height are time, temperature, and pressure [28]. One study compares methods of bonding microfluidic devices using chemical-assisted surface modification under mild conditions [29], while other work proposes an enhanced vacuum bagging technique for manufacturing substrate microfluidic devices and multilayer film devices. The latter shows that chips bonded under a vacuum pressure of 80–90 kPa can resist rupture pressures exceeding 550 kPa. However, a bonding time of 2 h or more is necessary to achieve optimal results [30].

The above studies indicate that an intrinsic trade-off exists between achieving high bonding strength and maintaining low deformation, i.e., a bonding performance or quality limitation exists that cannot be overcome using traditional approaches. This study, however, proposes the use of an innovative energy-gathering rib (ER) combined with microstructure design and optimization to address this paradox. The proposed ER consists of a tailored microstructure uniformly distributed on both sides of a microchannel. This ER is designed to improve overall bonding performance through enhanced structural design while resulting in only a minor increase in cost and complexity. Herein, simulation and experiments are combined based on the characteristics of the in-mold thermocompression bonding process. Initially, simulation investigates the influence of the ER on microchannel deformation, optimizes the ER structure, and establishes design principles. This is followed by experiments involving injection molding and thermocompression bonding that examine the bonding strength and microchannel deformation of ER microfluidic chips in relation to process parameters. Analysis of the morphology at the bonded interface follows to elucidate the working mechanism and principle by which the ER augments bonding strength.

2. Materials and methods

2.1. Materials

The basic material used in this study is Poly(methyl methacrylate) (PMMA, ACRYREX®, CM-205, Taiwan). The fundamental properties of this material can refer to the literature [26]. Prior to the injection molding process, PMMA was dried in a desiccant dryer (SHINI®, SCD-20U/30H, Taiwan) at 80 °C for a minimum of 8 h to avoid any important effects of moisture on the experiments.

2.2. Bonding strength

Leakage testing and burst pressure testing are employed to assess the bonding strength of the microfluidic chips. Leakage testing is conducted by applying pressure to the microfluidic chip and directly observing fluid leakage. The principle of burst pressure testing and the connection methods of various components are shown in Fig. 1(a). There, a microfluidic chip and connector are bonded using epoxy resin. The epoxy resin used in this study (5009, LEAFTOP, China) is a commercially available adhesive composed of two parts: Part A and Part B. Part A contains epoxy resin, fillers, and accelerators, while Part B consists of a curing agent, catalyst, and plasticizer. When bonding connectors to chips, both parts are mixed in a 1:1 ratio. The connector is then briefly immersed in the mixed solution to apply a thin layer and placed at the designated position on the chip, followed by curing (Fig. 1(b)). A pressure gauge (ConST211, China) with a range of 0–4 MPa and an accuracy of 0.05–0.2 % is used to record the pressure change curve and the peak pressure within the channel. To ensure a steady pressure increase within the channel, a microsyringe pump (HARVARD APPARATUS®, HA1100D, USA) is used to provide a constant flow rate of 2 μL/min.

2.3. Microchannel morphology

The quality of injection-molded microstructures is directly influenced by the processing quality of the core mold. Therefore, the accuracy of microstructure replication and the deformation of microchannels post-thermocompression bonding require quantification. An inverted optical microscope (Nikon Ti-2U, Japan) is used for characterizing microchannels and ER cross-sections. A super depth-of-field 3D microscope system (KEYENCE®, VHX-5000, Japan) is used to inspect the injection molding mold and to evaluate the quality of both injection molding and thermal bonding. The inspection parameters and settings include 200 × magnification, image stitching, and surround lighting. A combination of coatings and a modified measurement technique are used to eliminate the influence of optical transparency. A silver metal coating is prepared (current: 50 mA, type: directional, time: 300 s) using an ion sputtering deposition system (EM ACE200, LEICA, Germany). Then a combination of coaxial and ring illumination is employed, with the light intensity adjusted until the contours are clearly defined. The final contour line of the microstructure is derived by averaging ten equidistant contour lines. The deformation of the microchannel is calculated from the ratio of the cross-sectional area before and after bonding using Eq. (1) [22,26,27].

$$\partial = 1 - \frac{\Delta S_a}{\Delta S_b} \tag{1}$$

where ΔS_a is the cross-sectional area of the microchannel after bonding, ΔS_b is the cross-sectional area of the microchannel before bonding. Hence, $\Delta S_a / \Delta S_b$ is the bonded microchannel area ratio.

2.4. Scanning electron microscope

Scanning electron microscope (SEM, ZEISS®, Sigma 300, Germany) images are acquired to investigate the mechanism underpinning the bonding strength. The extra high tension (EHT) is set to 3 kV for morphology imaging, and the target material is platinum. This allows for the observation of surface morphology trends in the bonding region before and after bonding. Injection-molded chips are randomly selected for SEM imaging before bonding, while post-bonding samples are chosen from chips that undergo burst pressure testing and subsequently separate into two parts (the cover and the substrate). All samples are cleaned with deionized water to remove surface contaminants and residual burst test media (ink). Before imaging, the samples are coated with gold to enhance the electrical conductivity of the surface and avoid the charging effect. The sputter coater (Quorum®, SC7620, United Kingdom) operates for 45 s at 10 mA.

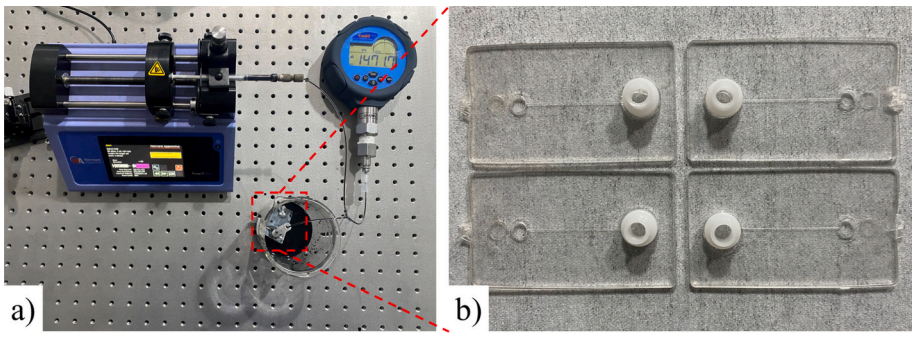

Fig. 1. (a) The testing apparatus for evaluating bonding strength, (b) detail showing the microfluidic chips with connector, adhered by epoxy resin. Notice that burst pressure testing utilizes a micro-syringe pump, a 1 mm diameter syringe, a pressure gauge, and a pathway that consists of appropriate micro-tubing.

3. Simulation and experimental details

3.1. Simulation description

Finite element analysis is frequently employed in the design of microchannel structures, typically to reduce mold manufacturing costs and time [31]. Here, a transient structural analysis in Ansys Workbench software simulates the deformation pattern of the microchannel during the thermocompression bonding process. The goal is to improve bonding performance by designing the ER, as depicted in Fig. 2. This simulation investigates how the cross-sectional shape (trapezoidal, rectangular), structural parameters (height, h), and position (distance to the microchannel, L_d) of the ER influence bonding performance. Table 1 presents the comprehensive simulation scheme.

Table 1
All parameter levels that are used for the simulation study of the ER.

Cross-sectional shape	L_d/μm	Height/μm	Width/μm
Rectangular Trapezoidal	150,200,400	100,200	400

3.2. Model

The ER is anticipated to enhance bonding strength and reduce microchannel deformation. For the microchannel deformation simulation study, a 2D planar model is employed, taking advantage of the symmetry of the microstructure (Fig. 2). A systematic mesh convergence analysis is performed using a mesh predominantly composed of quadrilateral elements, with element sizes ranging from 0.2 mm to 0.005 mm (Fig. 2(c)). This analysis determines that a mesh size of 0.02 mm (approximately 42,000–45,000 elements and 130,000 nodes) provides an optimal balance between computational efficiency and accuracy, with further refinement yielding diminishing returns (deformation change < 0.1 %, Section 4.1). The boundary conditions set are: A-bonding processes (bonding pressure, temperature, time); B-friction support; C-linear displacement. The simulation model and the boundary conditions setup for the thermocompression bonding of the ER are

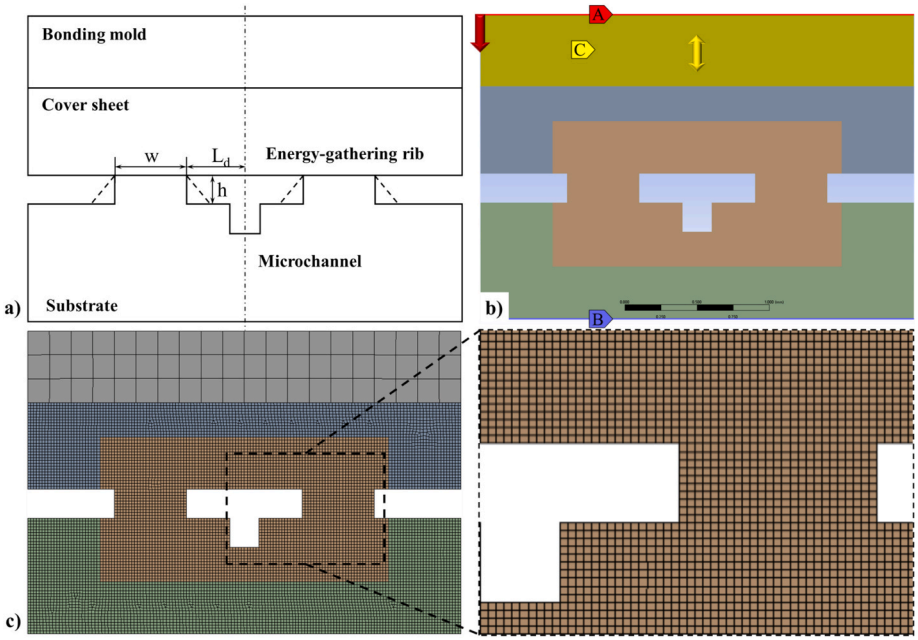

Fig. 2. (a) Schematic diagram of a microchannel with energy-gathering rib. The ER is an elevated microstructure, which is symmetrically distributed on both sides of the microchannel. The simulation investigates how the cross-sectional shape (trapezoidal, rectangular), the structural parameters (height: h, width: W), and the position (distance to the microchannel: L_d) of an ER influence the bonding performance. The deformation of the rectangular microchannel on the substrate is the object of observation. (b) Image showing the boundary condition of the simulation model (A-bonding pressure, B-friction support, C-linear displacement). The material properties of the bonding mold and chips are structural steel and PMMA, respectively. (c) Depiction of the mesh type, which is quadrilateral dominated and the optimized cell size, which is 0.02 mm.

depicted in Fig. 2(b). The boundary conditions are set using advanced process parameters from the literature and experimental conditions available for validation, including bonding pressure (1.7 MPa), temperature (106 °C), and time (4 min) [26]. The literature indicates that during the thermal bonding process, there is no temperature difference between the bonding interface and the mold surface, meaning that the temperature distribution across the chip is uniform. Consequently, during the simulation process, the bonding temperature is controlled by a specified global temperature. The material properties are configured with the PMMA CM 205 material table in the Ref. [26]. Referring to the experimental standards ASTMD2990-2001/ASTMD2990-2017, the parameters of the generalized Maxwell model of the material are determined by compression tests [27]. The material constitutive model employed in this study has been comprehensively validated through experimental testing in our previous work [27]. In that study, direct comparisons between measured and simulated stress–strain responses and deformation profiles under various loading conditions demonstrated excellent agreement (deviations < 10 %), confirming the accuracy and reliability of the constitutive parameters used in the present simulations. Building upon this validated material model, the current work focuses on mesh convergence analysis and boundary condition optimization to ensure numerical stability and computational efficiency for the specific geometric configurations investigated herein. To ensure consistency between the simulation and experimental results in this study, the following are incorporated: (1) employ a custom-built thermal bonding apparatus with temperature control accuracy of ± 1°C and pressure control accuracy of ± 0.05 MPa [26]; (2) use validated material constitutive equations, resulting in thermal bonding simulation errors of less than 10 % [27]; (3) apply appropriate boundary conditions for each case.

3.3. Injection molding

Following the simulation driven optimization, the ER of the microfluidic chip undergoes injection molding. The core of the injection molding is shaped with precision electric discharge machining (EDM) and grinding (Fig. 3(a)). The injection molding apparatus and mold temperature controller are the Arburg 370S (500–100) (Germany) and the AODE-05A (China), respectively. The injection molding parameters for the ER microchannel chip are derived from the process combination of the cross-electrophoresis microfluidic chip, as shown in Table 2 [27].

Table 2
The injection molding parameters for microfluidic chips.

Melt temperature/℃	Injection pressure/MPa	Injection speed/(cm^3/s)	Package pressure/MPa	Packaging and cooling time/s
260	180	45	100	25

3.4. Thermocompression bonding

As can be seen in Fig. 3(b), the thermocompression bonding experiments of the ER microfluidic chip are carried out on a proprietary platform. The bonding system can accurately regulate the surface temperature of the bonding cavity and deliver the bonding pressure via a servo electric cylinder. More detailed information is described in literature [26]. The detailed plan for single-factor thermocompression bonding is outlined in Table 3.

4. Results and discussion

4.1. Design and optimization

Mesh convergence analysis is a crucial analytical procedure prior to finite element simulation [32,33]. The impact of mesh size on the simulation outcomes is plotted in Fig. 4(a). Given the different scale mesh sizes (0.2, 0.1, 0.05, 0.02, 0.005 mm), normal and exponential scale x-axes are used for plotting and visual enhancement, respectively. As observed, the maximum deformation of the microchannel progressively increases with the reduction of mesh size, underscoring the necessity of mesh convergence analysis. When the mesh size reaches 0.02 mm, the growth rate of the deformation slows down, indicating that the influence of mesh quality on the simulation results is progressively decreasing. With cell size reduction from 0.02 mm to 0.005 mm, the maximum deformation of the microchannel increases by only 0.1 %, which is negligible and lies within the tolerance level of the process.

Table 3
Experimental conditions used for the thermocompression bonding of the ER.

Bonding temperature (℃)	Bonding pressure (MPa)	Bonding time (s)	Detection and analytics
97,100,103,106	0.65 1 1.35 1.7	240	Binding Strength Microchannel Deformation Surface Morphology

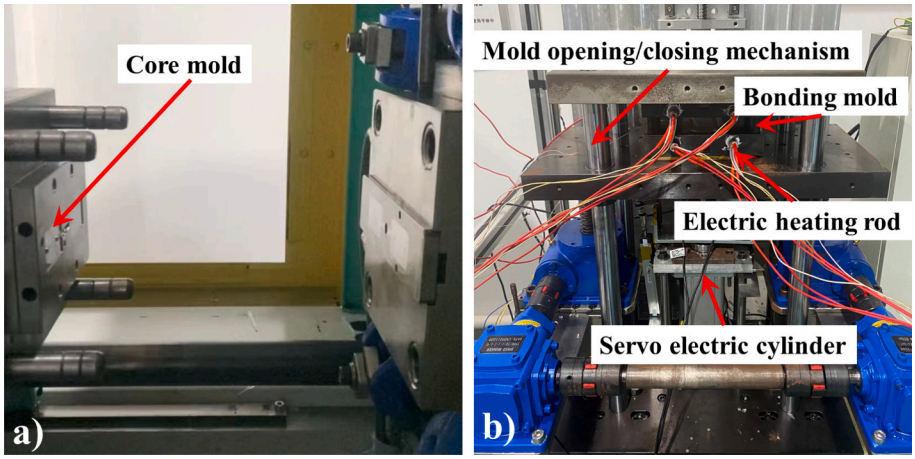

Fig. 3. (a) The injection molding mold for ER microfluidic chips. The core of the injection molding is shaped with precision electric discharge machining (EDM) and grinding. (b) The thermocompression bonding system for microfluidic chips. The mold temperature is provided by electric heating rods, when the chips temperature is provided by thick film heater as shown in literature [26].

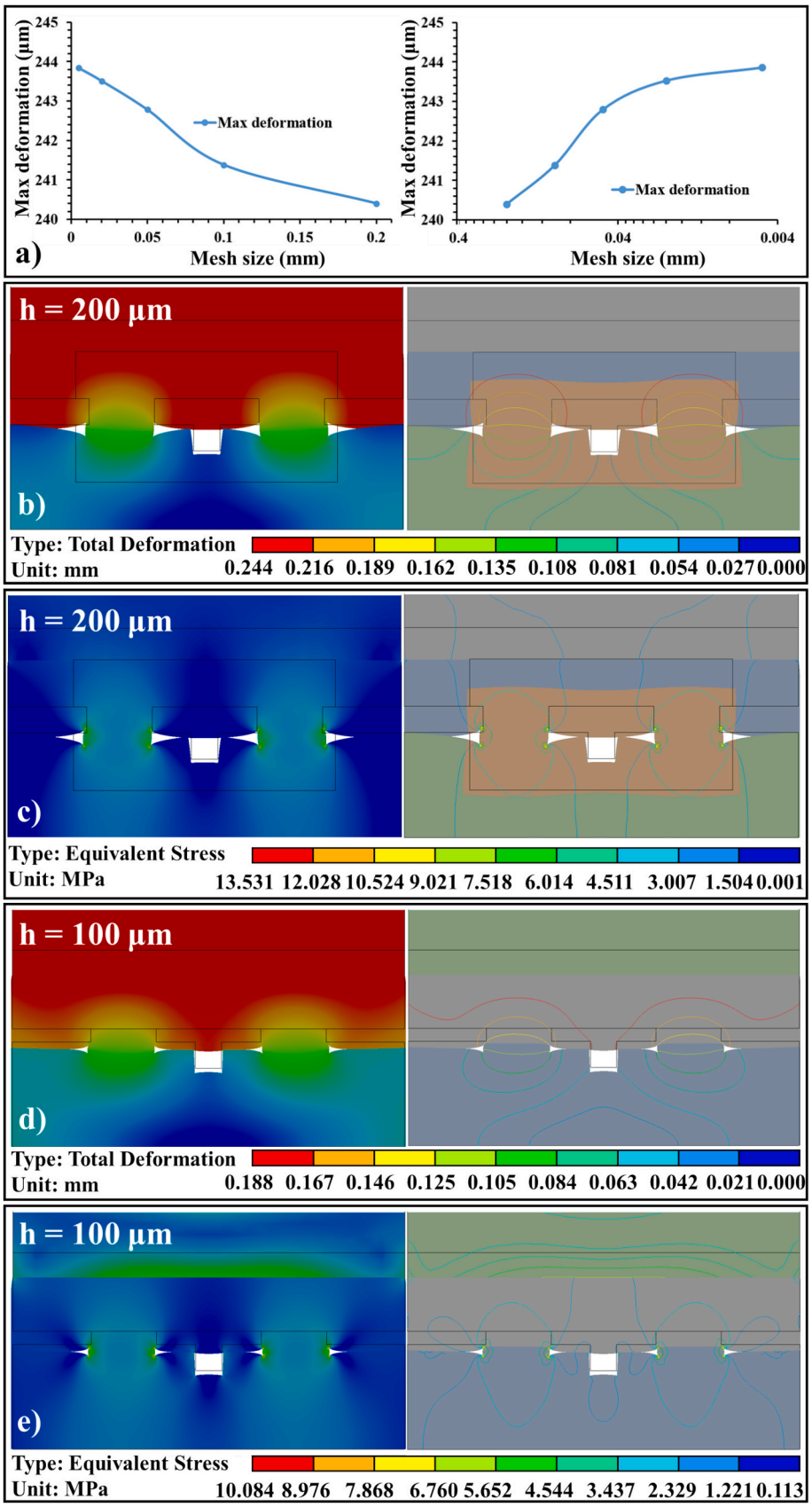

Fig. 4. (a) The trend of microchannel maximum deformation with mesh size on normal and exponential scaled x-axis. Notice that when the mesh size is 0.02 mm, the growth rate of the most significant deformations slows down, pinpointing the decrease of the influence of mesh quality on the simulation results. Depiction of simulation results of microchannel deformation (b, d) and equivalent stress distribution (c, e) for a microchannel. The 200 μm high ER transforms the rectangular

microchannel cross-section into a trapezoidal shape. The equivalent stress distribution diagrams show that the stresses are predominantly concentrated on both sides of the ER. When the height of the ER is reduced to 100 μm, the microchannel deformation and the stress concentration significantly ameliorate.

Consequently, a mesh size of 0.02 mm is considered appropriate for conducting the simulation study in this work.

To evaluate the design method and principles of the ER, a qualitative simulation analysis is conducted, followed by experiments to further scrutinize the benefits of the ER. It is important to note that the FEA simulation study incorporates the impact of the position and structural parameters of the ER on microchannel deformation, contributing to structure optimization and establishment of design principles. The primary objective of the ER design is to minimize microchannel deformation. Therefore, the bonding pressure is determined with reference to the in-mold thermocompression bonding process in the literature [26]. The reported deformations of trapezoidal microchannels with top and bottom widths and heights of 100, 40, and 40 μm, respectively, reach 68.83 % when the bonding temperature, pressure, and duration are 106 °C, 1.7 MPa, and 4 min. These process parameters lead to substantial deformation or even complete failure of the microchannels. To investigate the contribution of the ER to bonding performance, a microchannel deformation simulation is subsequently performed using these process parameters.

The impact of the ER height on microchannel deformation is illustrated in Fig. 4(b) and (d). Figs. 4(c) and (e) display the microchannel deformation and stress distribution when the ER height is 200 μm and 100 μm, respectively. The finite element simulations reveal the dependence of microchannel deformation and stress concentration on the ER height *h*. Despite employing bonding parameters reported to cause microchannel collapse, the tall ER remains incompletely densified and instead induces a parasitic bending moment that distorts the rectangular microchannel into a trapezoidal cross-section. This deformation arises from asymmetric lateral constraint: the compliant ER accommodates compressive strain through lateral expansion, generating transverse tensile stresses that concentrate at the ER sidewall interface. The equivalent stress peaks at 13.53 MPa along the ER lateral edges—a manifestation of elastic stress singularity at re-entrant corners, as can be seen in Figs. 4(b) and (d). The equivalent stress distribution diagrams indicate that stresses are predominantly concentrated on both the sides of the ER. Consequently, further increases in bonding pressure or bonding temperature would only exacerbate this deformation. All the aforementioned phenomena demonstrate that the ER height is excessively high in this case. When the height of the ER is reduced to 100 μm, the microchannel deformation and the stress concentration are significantly ameliorated. The maximum deformation decreases to 0.188 mm (23 % reduction), while peak stress attenuates to 10.08 MPa (25 % reduction), as depicted in Figs. 4(c) and (e). In this case, the sidewalls of the microchannels show no significant tilting or deformation. Moreover, the microchannel deformation with the ER structure is less than 10 % compared to the initial design. However, under identical bonding conditions, the microchannel deformation reported in the literature reaches 68.83 %, clearly demonstrating that the presence of the ER significantly reduces microchannel deformation. On the other hand, although the maximum stress concentrated around the four corners of the ER decreases from an initial value of 13.5 MPa to 10.1 MPa, the stress concentration remains significant. Simultaneously, phenomena such as “shoulder corners” or gaps on both sides of the ER persist, preventing complete channel sealing—a consequence of residual surface curvature (Figs. 4(d) and (e)). The presence of these gaps negatively impacts bonding strength, thus further optimization of the ER structure is necessary to eliminate the effects of gaps.

Similar to the height, the distance between the ER and the microchannel axis influences the deformation and the bonding strength. The impact of the ER position on microchannel deformation is illustrated in Fig. 5. Systematic variation of ER-to-microchannel spacing (Fig. 5(a–c)) reveals a design trade-space: when the ER is too close to the microchannel (L_d < 150 μm), the gaps connect to the microchannel, leading to an increase in the microchannel volume (Fig. 5(a)). This type of enlargement in the microchannel reduces the nominal flow rate, and negatively affects the analytical results [3]. Additionally, as shown in Fig. 5(b), the sidewalls of the microchannels bend under stress, thereby exacerbate the deformation. Meanwhile, as depicted in Fig. 5(c), the negative impact of the ER on deformation progressively decreases with an increased spacing between the ER and the microchannel. Consequently, deformation can be effectively mitigated by suitably increasing the distance between the ER and the microchannel. Evidently, the position and the height of the ER are the two named variables that need to be optimized. The simulation results clearly indicate that the height and position of the ER are optimum when set to be half of the microchannel depth, and also over double of its width, respectively. Under this configuration, the ER's compliant zone decouples substrate stresses without inducing parasitic deformation modes.

Despite minimizing the influence of height and position, the presence of gaps may also hinder the improvement of bonding strength. The proposed solution is the use of a trapezoidal ER structure. Fig. 5(d–g) shows the simulation results of the ER shape on the microchannel deformation, the gaps, and the stress distribution. The results reveal that transitioning from rectangular to trapezoidal ER cross-sections (Fig. 5 (d–g)) reduces gap volume through graded contact pressure distribution: the tapered profile increases effective contact width by approximately 50 %, redistributing pressures over a larger area and altering the tendency to accommodate compressive strain through lateral expansion. Simultaneously, the sloped sidewalls redirect principal stress orientations away from the microchannel substrate, mitigating residual stress transmission—maximum substrate-side stress decreases from 10.1 MPa (rectangular) to 6.5 MPa (trapezoidal), as shown in Fig. 5(g). The substrate side, where the microchannels are located, shows no obvious stress concentration (Figs. 5(e) and (g)) even with a maximum residual stress of 12.1 MPa. These results demonstrate that the proposed trapezoidal shape for the ER can effectively mitigate residual stress on the microchannel side and prevent bending deformation.

Following a series of optimization simulations, Fig. 5(h–j) displays the final structure of the ER along with comparison results. Compared to the rectangular microchannel, the deformation of the ER microchannel is reduced by 16.47 %. Moreover, the thermocompression bonding deformation of a trapezoidal microchannel is established and simulated in accordance with the literature. In comparison, the deformation of the ER microchannel decreases by 35.13 %. It is clear that the ER offers benefits in reducing microchannel deformation. These improvements derive from three synergistic mechanisms: (1) bending-dominated compliance of the ER, (2) stress diffusion via trapezoidal geometry eliminating corner singularities, and (3) spatial decoupling of bonding loads from fluidic structures. It should be noted that while the initial simulation work served as a valuable design tool to explore the ER concept and establish design guidelines, the experimental characterization presented next section represents the ultimate validation for practical engineering applications.

4.2. Experimentation and performance

The ER microchannel chip and the injection molding core are shown in Fig. 6 (a) and (b) respectively. They are designed in accordance with the simulation results from Section 4.1. The injection molding core is crafted through precision electric discharge machining (EDM). This straightforward process ensures precise control while maintaining low material costs. This section presents the experimental verification of the ER microstructure's enhancement of thermocompression bonding performance. Given this objective, the tolerance for dimensional errors in

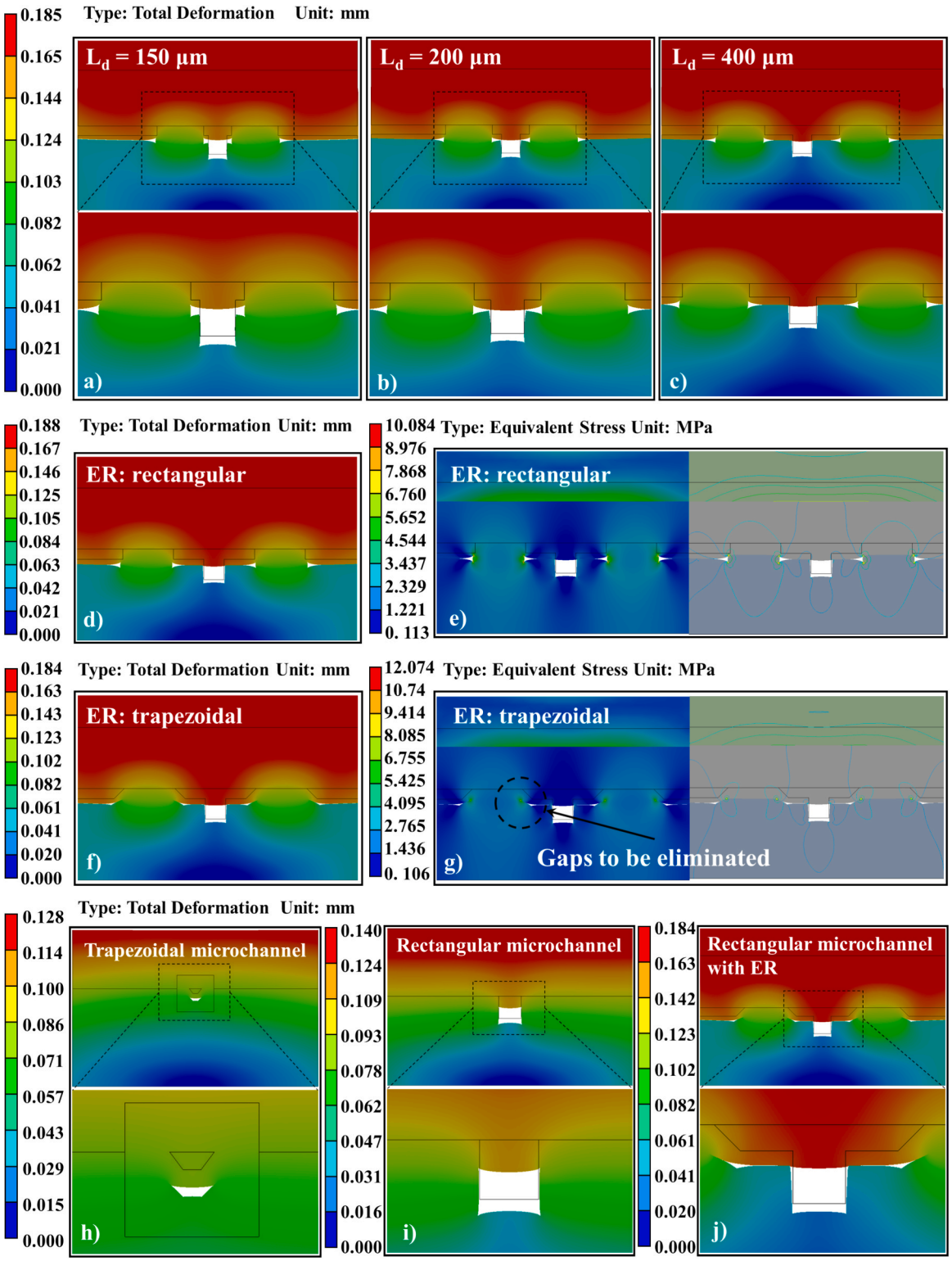

Fig. 5. Simulation results of the ER position ((a)L_d = 150, (b) 200, (c) 400 μm) impact on the microchannel deformation. (a) The gaps connect to the microchannel when the ER is too close to the microchannel, leading to an increased microchannel volume. (b) The sidewalls of the microchannels bend under stress, thereby exacerbate the deformation. (c) Microchannels are unaffected by the ER. Effect of (d) rectangular and (f) trapezoidal ER on microchannel deformation and stress distribution (e, g). The trapezoidal ER helps to eliminate gaps and reduces stress concentrations compared to rectangular ER. Notice that compared to the trapezoidal microchannel, the deformation of the ER microchannel decreases by 35.13 %. (j) Simulation result showing that compared to the rectangular microchannel, the deformation of the ER microchannel is reduced by 16.47 %.

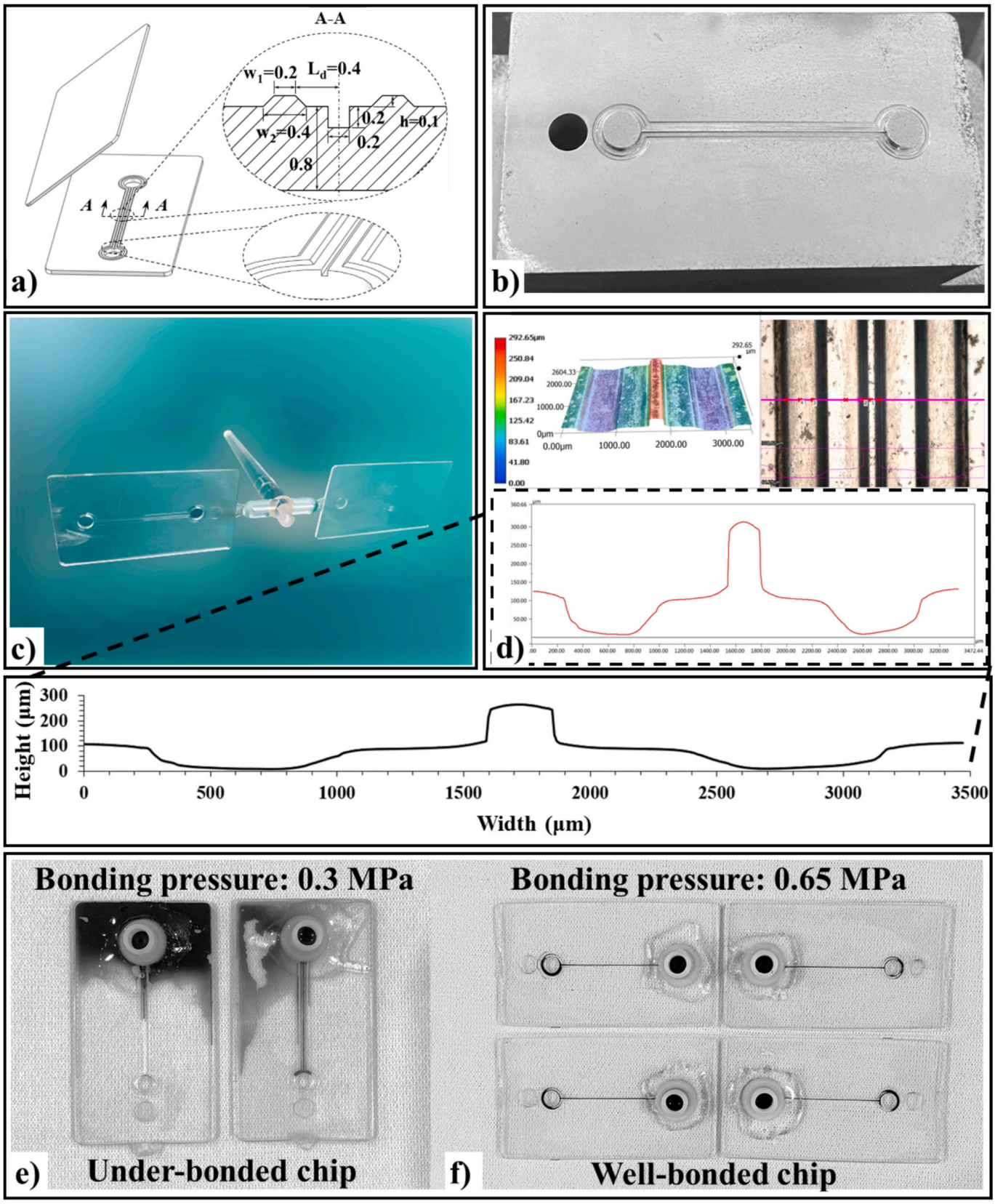

Fig. 6. (a) Schematic of the final designed microfluidic chip and of the characterization dimensions of the ER. (b) The injection mold core of the ER microfluidic chip that is prepared by precision EDM and grinding. (c) The injection molded ER chip; (d) The microstructural morphology and profile of injection mold core. Notice that the super depth-of-field microscopy confirms that the mold core and microfluidic chip meet the bonding requirements, when tolerance for the structural dimensional errors is ± 20 mm. (e) Photo of the under-bonded microfluidic chips with bonding pressure 0.3 MPa that fail leakage test. (f) Photo of well-bonded microfluidic chips with bonding pressure 0.65 MPa showing no signs of leakage.

the structure is set at ± 20 μm.

The injection molded microfluidic chip and microstructural morphology of the mold core are shown in Figs. 6(c) and (d) respectively. Super depth-of-field microscopy confirms that both the mold core and microfluidic chip meet the bonding requirements described in the previous paragraph. The profile line of the injection-molded chip is utilized as the basis for calculating the deformation, excluding any manufacturing errors.

Subsequent bonding experiments were conducted involving the thermocompression bonding of the microfluidic chip. The results show that the introduction of the ER alters both the process window and the optimal bonding parameters. Previous studies have demonstrated that microchannels without ER structures can be sealed using a bonding temperature of 103 °C and a pressure of 0.3 MPa [26]. However, to successfully seal the shoulder corners in ER-enhanced chips, the bonding pressure needs to be increased to approximately 0.65 MPa. Simulation results clearly indicate that under these lower bonding process conditions, shoulder corners exist on both sides of the ER, which was confirmed by leakage testing experiments. The results demonstrate that at 0.3 MPa, adequate sealing cannot be achieved at the shoulder corners within the designated bonding temperature range (Fig. 6(e)). Well-bonded microfluidic chips can be obtained with an increase in pressure (Fig. 6(f)), which enables the detection of burst pressure and microchannel deformation.

The variation of microchannel deformation and bonding strength with respect to bonding temperature and pressure is shown in Fig. 7. The influence of bonding temperature on microchannel deformation is exponential, and bonding temperatures approaching the glass transition temperature (T_g) of the polymer clearly influence the microchannel deformation. In contrast, both microchannel deformation and bonding strength increase linearly with bonding pressure (Figs. 7(b) and (c)).

Multiple indicators can be employed to assess overall bonding performance, with bonding strength being a primary metric. Our previous work [26] has demonstrated that microchannel morphology and bonding strength exhibit different responses to various process parameters, highlighting the necessity of identifying an optimal process parameter combination to achieve optimal performance. That study demonstrated that compared to microchannels without the ER structure, the bonding strength increased by ~ 123 % and microchannel deformation decreased by ~ 6 % under identical process parameters [26]. It should be emphasized that this bonding performance surpasses the vast majority of the reported performances for most applications [29,34]. When microchannel deformation is 12.62 % (less than the reported 15 % threshold), the bonding strength increases by 160 % to 1.56 MPa [26,35]. In the present study, when the bonding temperature is 103 °C and the bonding pressure is 1.7 MPa, the burst pressure exceeds the measurement capacity of the test system (Fig. 7(d)), with leakage occurring in the test line, clearly demonstrating that the weakest link in the test system is no longer the bonded microfluidic chip. Cross-sectional analysis was performed using both optical microscopy (Fig. 7(e)) and three-dimensional depth-of-field microscopy (Fig. 7(f)) to provide comprehensive characterization of the bonding performance. The optical microscopy images (Fig. 7(e)) clearly show the microchannel and ER structures after bonding at representative process conditions. Notably, the ER exhibits excellent structural integrity without shoulder corners on either side, indicating uniform stress distribution and effective energy absorption during the thermocompression bonding process. This smooth ER profile confirms that the structure successfully prevents localized stress concentration that could otherwise lead to excessive channel deformation. The 3D topographical measurements (Fig. 7(f)) provide quantitative validation of the bonding quality across different process parameters. The color-coded height maps reveal that the microchannel maintains its designed geometry with minimal deformation, while the ER consistently shows well-defined profiles that closely match the original design. These direct cross-sectional measurements corroborate the quantitative deformation data presented in Fig. 7(a–b) and provide visual confirmation of the excellent bonding performance achieved through ER-assisted thermocompression bonding. The consistency between optical and depth-of-field microscopy observations, combined with the bonding strength measurements, confirms that the optimized process window achieves the dual objectives of high bonding strength and minimal channel deformation, meeting the stringent requirements for microfluidic applications.

The comparative analysis of different PMMA bonding methods reveals several significant findings (Table 4). The comparative analysis (Table 4) must be interpreted considering methodological variations across studies. The ER assisted thermal bonding method achieves exceptional burst strength (1.56 MPa) while maintaining precise control over processing parameters. This represents a substantial improvement over conventional thermal bonding (600 kPa) and other methods, as for example solvent-assisted bonding (655–1000 kPa). The enhanced performance is attributed to the structural design innovation (ER). While some film-assisted methods report higher absolute burst pressures, they require additional materials and processing steps, increasing cost and complexity. The key advantage of our approach is the simultaneous optimization of bonding strength and microchannel integrity through structural design rather than process intensification or chemical modification. In addition to being easy to implement, this work offers several practical benefits over existing approaches. Unlike film-assisted methods, this technique eliminates the need for additional materials, whilst the absence of chemical solvents not only simplifies the process, but it also prevents potential contamination risks that are common in solvent-based bonding.

4.3. Bonding mechanism

The process-property harmonization principle is to set the bonding temperature at 5–8 °C below the T_g, in combination with the use of the lowest possible bonding pressure and time. Bonding pressure is the only adjustable factor that does not directly affect microchannel deformation or decrease in productivity. It is known that traditional thermal bonding faces challenges in achieving synergistic control of bonding performance, where improving the bonding process parameters simultaneously leads to increased bonding strength and microchannel deformation, and vice versa. However, optimizing the process alone cannot simultaneously balance bonding strength and microchannel deformation. To address this issue, the ER microstructure proposed in this work directly leads to a geometric increase in bonding pressure, since the reduced contact area concentrates the bonding pressure on the ER, thereby increasing the bonding strength. Hence, the ER microstructure increases bonding strength while reducing microchannel deformation.

The interface of the ER after bonding is shown in Fig. 8. SEM micrographs reveal that the surface roughness of the ER increases post-bonding. This roughness is influenced by both bonding temperature and pressure. The exfoliated polymer layers visible in the images showcase the intricate processes occurring at the bonding interfaces, including the interdiffusion and the entanglement of molecular chains, which are promoted by heat and contribute to the observed increase in surface roughness. These results support the hypothesis that the ER enhances the bonding strength by promoting chain entanglement. This is because the energy required to break or form atomic and molecular bonds determines the bonding strength, and is influenced by temperature, pressure, duration, and the properties of the materials involved in the process. Specifically, molecular diffusion is a process that involves the movement of polymer chains across an interface, and is facilitated by heat, which encourages the integration of the two substrates. Entanglement refers to the complex interweaving of polymer chains at the interface and plays a crucial role in the enhancement of bonding strength. The observed surface roughness trends (Fig. 8) correlate quantitatively with burst pressure measurements (Fig. 7), validating this interpretation. Meanwhile, several molecular dynamics (MD) simulation

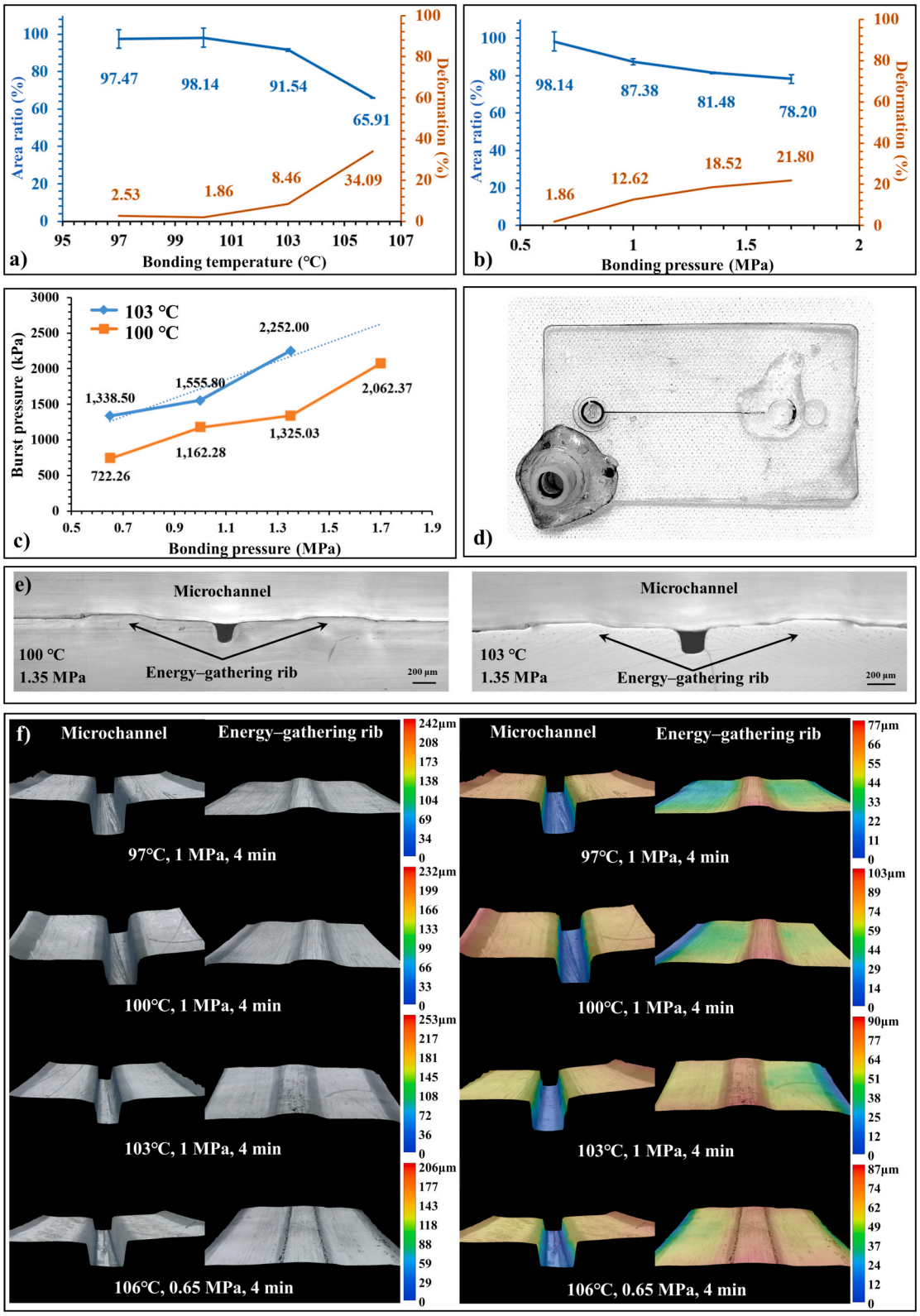

Fig. 7. Effect of (a) bonding temperature and (b) bonding pressure on microchannel deformation (bonding pressure, 0.65 MPa). Notice that the influence of bonding temperature on microchannel deformation is exponential, and a bonding temperature close to the glass transition temperature (Tg) of the polymer clearly exacerbates the microchannel deformation. The microchannel deformation and bonding strength increase analogously with bonding pressure. (c) Effect of bonding temperature and bonding pressure on bonding strength. (d)Picture showing that when the bonding temperature is 103 °C and the bonding pressure is 1.7 MPa, the burst pressure cannot be measured, due to leakage occurring at the test line, i.e. the connecter fell off. (e) Cross-sectional optical microscopy images of the bonded microfluidic chip showing the microchannel and ER structures. The ER maintains excellent structural integrity without shoulder angles on both sides, demonstrating effective stress distribution during the bonding process. (f) 3D depth-of-field microscopy characterization of bonded microchannels and ERs under different process conditions (left panels show grayscale images; right panels show topographical profiles).

Table 4
The different bonding methods for PMMA-based microfluidic chip in terms of process, burst strength, and efficiency.

Method	Material	Effective parameters	Burst pressure	Deformation	Supplementary	Ref.
Film-assisted thermal bonding	PMMA-TPE, PMMA-PMMA	Bonding time: 15 min. Bonding temperature: 84℃ (PMMA), 70℃ (TPE). Bonding pressure: 2.4 MPa (PMMA), 1.6 MPa (TPE).	1000 kPa	/	/	[36]
Film-assisted thermal bonding	PMMA-film-PMMA	Bonding time: 10 min.	Over 2 MPa	/	Polyethylene terephthalate + UV curing adhesive	[37]
Solvent bonding	PLA-PMMA	Bonding time: 30 min. UV light. Annealing temperature: 50 ℃	1.352 MPa	/	/	[38]
Solvent-assisted thermal bonding	PMMA-PMMA	Bonding time: 40 min. Bonding temperature: 70 ℃. Bonding pressure: 10 kPa.	1000 kPa	/	Multilayer bondingPropan-2-ol, (IPA, poisonous)	[39]
Solvent-assisted thermal bonding	PMMA-PMMA	Bonding time: 20 min. Bonding temperature: 60 ℃.	655 kPa	/	/	[40]
Solvent-assisted thermal bonding	PMMA-PMMA	Bonding time: 15 min. Bonding temperature: 68 ℃.	660 kPa	/	Isopropyl alcohol (poisonous)	[41]
Thermal bonding	PMMA-PMMA	Bonding time: 5 min. Bonding temperature: 103 ℃. Bonding pressure: 0.3 MPa	600 kPa	15 %	Highly dynamic tempered in-mold thermocompression bonding	[26,42]
Thermal bonding	PMMA-PMMA	Bonding time: 5 min. Bonding temperature: 109 ℃. Bonding pressure: 1.7 MPa	1.77 MPa	7 %	Deformation compensation	[27]
Thermal bonding	PMMA-PMMA	Bonding time: 5 min. Bonding temperature: 103 ℃. Bonding pressure: 0.65 MPa	1.56 MPa	12.6 %	Structural design	This work
		Bonding time: 5 min. Bonding temperature: 103 ℃. Bonding pressure: 1.7 MPa	Over 2.25 MPa	21.8 %		

Note: Direct quantitative comparison is challenging due to variations in: (1) microchannel geometries (width, depth, aspect ratio), (2) bonding area, (3) measurement methods, and (4) reported metrics. Where deformation data is unavailable ("/" entries), it was either not reported in the original studies or measured using different criteria that prevent direct comparison.

studies provide additional molecular-level insights that corroborate our experimental observations [43]. Zhou et al. [44] conducted MD simulations specifically on PMMA thermal bonding for microfluidic applications, showing that molecular penetration occurs predominantly near the interface region and that bonding pressure significantly influences the diffusion coefficient and joining energy at the molecular level. Their computational results support our experimental findings that the unique structural design of the ER facilitates geometric amplification of bonding pressure, thereby promoting chain interdiffusion and entanglement. Ge et al. [45] performed large-scale MD simulations of polymer thermal welding and demonstrated that interfacial bonding strength is directly proportional to the areal density of entanglements formed across the interface. Their simulations revealed that sufficient interfacial entanglements are essential to prevent catastrophic chain pullout and achieve bonding strength comparable to bulk material, consistent with our observation that increased surface roughness (indicating enhanced chain interdiffusion) correlates with improved bonding performance.

Enhancing bonding performance can be directly and effectively achieved by increasing the bonding temperature and pressure, and by extending the bonding time. The mechanism responsible for generating bonding strength through thermocompression can be summarized as follows. The T_g of a polymer signifies the onset of random thermal mobility of its molecular segments, which is macroscopically observed as a phase transition from a solid to a viscoelastic state. A bonding temperature approaching the T_g, provides enough energy for interdiffusion, entanglement, and van der Waals forces at the bonding interface. The bonding pressure and time promote the interdiffusion and the entanglement of molecular segments. Therefore, the unique structural design of the ER facilitates a geometric increase in bonding pressure, and subsequently enhances the bonding strength. Simultaneously, the dual benefits of high bonding strength and low microchannel deformation are achieved with only a minor increase in the production cost.

The improvement in bonding strength is primarily due to enhanced surface fusion (surface diffusion) of the PMMA substrates, which is facilitated by the locally concentrated compressive stress generated by the ER structure. More specifically, the ER structure serves as the means to significantly increase the local compressive stress at the bonding interface. This concentrated stress field creates favorable conditions for molecular-level bonding. Enhanced surface diffusion and chain entanglement are the fundamental mechanism and root cause of the bonding strength improvement at the microscopic level. Under thermocompression bonding conditions, the locally elevated compressive stress provided by the ER structure promotes these processes. It is important to emphasize that the compressive stress itself does not directly provide the bonding strength through mechanical compression. Rather, the elevated local stress acts as a driving force that promotes surface diffusion and molecular-level fusion. Once the bonding process is complete and the compression is removed, the bonding strength is maintained by the intermolecular forces and chain entanglement resulting from the enhanced surface diffusion, not by residual compressive stress.

This discussion elucidates why the ER structure can significantly enhance bonding strength, while reducing microchannel deformation, and provides a summary of the mechanism of bonding strength formation. This allows a set of design principles for the ER structure to be established as follows: 1) set the width and spacing at 2 × the microchannel width, 2) set the height at 1/2 the microchannel height, and 3) employ a trapezoidal cross-section. During the thermal bonding process, the ER ribs, which are uniformly distributed around the microchannels, initially come into contact with the cover sheet and undergo deformation under pressure, thereby generating bonding strength. Consequently, this results in an asymmetric distribution of localized stress concentrations around the ER ribs, which is the primary cause of macroscopic deformation as shown in Fig. 4. It is important to emphasize that although the presence of ER ribs leads to slight macroscopic deformation, they reduce microchannel deformation while enhancing bonding strength compared to the traditional channels, as demonstrated

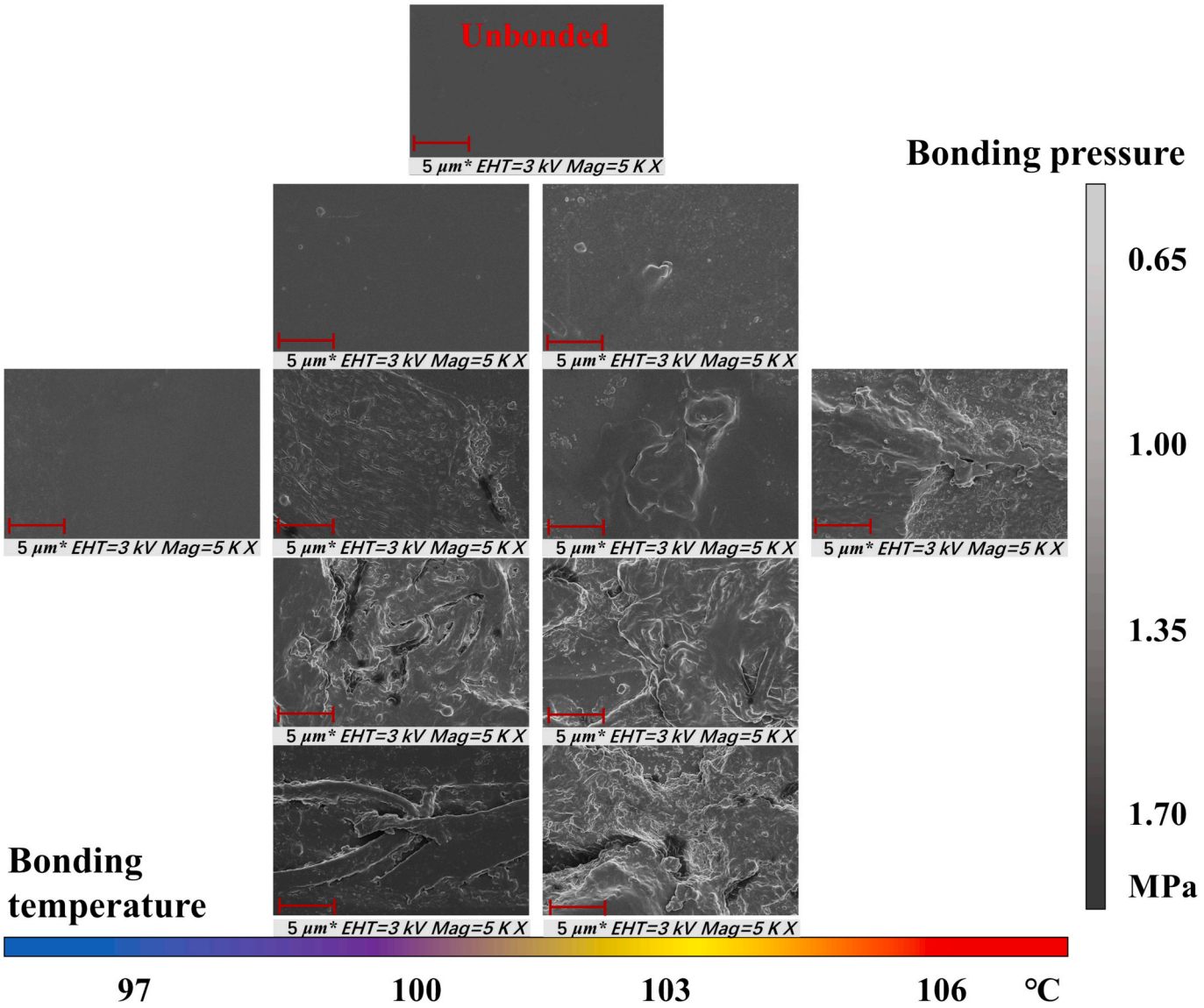

Fig. 8. Diagram showing the variation of the ER bonding interface, for different bonding pressures and temperatures. Notice that there is an increasing roughness between the ER bonding interface. This roughness is affected by both bonding temperature and pressure. However, the bonding pressure and temperature promote the interdiffusion and the entanglement of molecular segments. Therefore, the unique structural design of the ER, facilitates a geometric increase in bonding pressure, and subsequently enhances the bonding strength.

in Fig. 7. Considering the application scenarios of microfluidic chips, the focus of bonding performance clearly lies on the microchannel deformation and the bonding strength. The limitations of the ER lie in the space occupied by the continuous expansion of the complex microchannel networks and the potential for higher mold costs. This is because the volume of the ER and the distance between the ER and the microchannels will significantly increase the proportion of the microchannel area on the chip.

5. Conclusions and prospects

This work clearly demonstrates that the design of the energy-gathering rib significantly enhances the thermocompression bonding performance of microfluidic chips. The experimental results show that the ER improves the thermocompression bonding strength while simultaneously reducing microchannel deformation of the microfluidic chip. Using optimal bonding parameters, the ER microfluidic chip exhibits a bonding strength of 1.34 MPa, with a microchannel deformation of 8.46 %. Compared to conventional designs, bonding strength increases by 123 %, while microchannel deformation decreases by more than 6 %. Under conditions of comparable microchannel deformation, the bonding strength increases by more than 160 % to a value of 1.56 MPa.

FEA simulation successfully elucidates the principles that govern the influence of the ER structure on the microchannel deformation, as well as the structural design. The results demonstrate that microchannel deformation responds differently to individual ER structures. Additionally, the coordination between ER height and position directly influences the microchannel deformation. Furthermore, the shape of the ER is interconnected with the distribution of stress and shoulder corners. Consequently, for the structural design of the ER, it is necessary to set the width and the spacing at twice the width of the microchannel, the height at half the height of the microchannel, and employ a trapezoidal cross-section.

The observed evolution of interfacial morphology sheds light on the mechanism of thermocompression bonding strength formation, providing a theoretical foundation and a reference for the advancement of the commercialization of microfluidic chips. The different

mechanisms and trends by which thermocompression bonding factors affect bond strength suggest the existence of optimal bonding parameters. These parameters guide the fabrication of the ER to achieve a substantial increase in bonding pressure via a unique structure and enhance bonding performance. Under optimal conditions, the ER significantly enhances bonding performance through its unique structure. However, the ER increases the area occupied by the microchannel network and the volume of the microfluidic chip. Despite the promising results, several challenges must be addressed before widespread implementation. First, the addition of ER structures increases mold complexity, particularly for chips with dense microchannel networks, potentially raising fabrication costs. Second, while this study focused on PMMA, the generalizability of the optimized parameters to other polymers remains to be established. Nevertheless, this work provides a proof-of-concept framework that can guide similar studies with other polymers. Third, complex channel geometries may require adaptive ER placement algorithms. Future work should focus on three key directions: (1) development of computational design tools that can automatically optimize ER placement and dimensions for arbitrary microchannel networks; (2) extension of the ER concept to high aspect-ratio microchannels which present unique bonding challenges. Wherever a more detailed microchannel application is required, as for example in biofunctionalized microchannels, more research is needed that will focus on new process methods to amplify the bonding performance of the microchannels with high depth-to-width ratios.

This work not only underscores the benefits of traditional and in-mold thermocompression bonding, but also serves as a valuable reference for accelerating the commercialization of microfluidic chips, as the overall bonding quality is significantly improved with minimal increase in cost.

CRediT authorship contribution statement

Baishun Zhao: Writing – review & editing, Writing – original draft, Formal analysis. **Dimitrios Kontziampasis:** Writing – review & editing, Formal analysis. **Zhiyu Yang:** Resources. **Bingyan Jiang:** Project administration, Funding acquisition. **Wangqing Wu (吴旺青):** Writing – review & editing, Funding acquisition, Conceptualization, Resources. **Dou Zhang:** Supervision, Resources, Methodology, Formal analysis.

Declaration of competing interest

The authors declare that they have no known competing financial interests or personal relationships that could have appeared to influence the work reported in this paper.

Acknowledgements

The authors acknowledge the financial support given by the National Natural Science Foundation of China, China (Key International (Regional) Joint Research Program (No. 51920105008), Normal project (No. 52575469 and 51875582)), the Natural Science Foundation of Changsha Municipality, China (No. kq2402215), the Huxiang Young Talents Program of Hunan Province, China (No. 2019RS2003), and the Open Research Fund of State Key Laboratory of Precision Manufacturing for Extreme Service Performance, Central South University, China (No. ZZYJKT2023-11).

Appendix A. Supplementary data

Supplementary data to this article can be found online at https://doi.org/10.1016/j.matdes.2026.115448.

Data availability

Data will be made available on request.

References

[1] S. Aralekallu, R. Boddula, V. Singh, Development of glass-based microfluidic devices: a review on its fabrication and biologic applications, Mater. Des. 225 (2023), https://doi.org/10.1016/j.matdes.2022.111517.
[2] M. Refatul Haq, B. Mazinani, V. Subramanian, H. Schift, Room temperature imprinting of water-based microparticulate inks for realizing glass microfluidic channels, Mater Des 242 (2024) 112982. https://doi.org/https://doi.org/10.1016/j.matdes.2024.112982.
[3] C.W. Tsao, Polymer microfluidics: simple, low-cost fabrication process bridging academic lab research to commercialized production, Micromachines (basel) 7 (2016), https://doi.org/10.3390/mi7120225.
[4] C. Liu, X. Xu, Droplet microfluidics for advanced single-cell analysis, Smart Med. 4 (2025) e70002, https://doi.org/10.1002/smmd.70002.
[5] M.A. Alzoubi, O. Al-Ketan, J. Muthusamy, A.P. Sasmito, S. Poncet, Mixing performance of T-shape micromixers equipped with 3D printed Gyroid matrices: a numerical evaluation, Results Eng. 17 (2023), https://doi.org/10.1016/j.rineng.2022.100811.
[6] B. Xue, Y. Geng, Y. Yan, G. Ma, D. Wang, Y. He, Rapid prototyping of microfluidic chip with burr-free PMMA microchannel fabricated by revolving tip-based micro-cutting, J. Mater. Process. Technol. 277 (2020) 116468, https://doi.org/10.1016/j.jmatprotec.2019.116468.
[7] C. Dincer, R. Bruch, E. Costa-Rama, M.T. Fernandez-Abedu, A. Merkoci, A. Manz, G.A. Urban, F. Guder, Disposable Sensors in Diagnostics, Food, and Environmental Monitoring, ADVANCED MATERIALS 31 (2019). https://doi.org/10.1002/adma.201806739 WE - Science Citation Index Expanded (SCI-EXPANDED).
[8] H. Šípová-Jungová, L. Jurgová, E. Hemmerová, J. Homola, Interaction of Tris with DNA molecules and carboxylic groups on self-assembled monolayers of alkanethiols measured with surface plasmon resonance, Appl. Surf. Sci. 546 (2021) 148984, https://doi.org/10.1016/j.apsusc.2021.148984.
[9] Y. Song, Y. Jeong, T. Kwon, D. Lee, D.Y. Oh, T.J. Park, J. Kim, J. Kim, S. Kwon, Liquid-capped encoded microcapsules for multiplex assays, Lab Chip 17 (2017) 429–437, https://doi.org/10.1039/c6lc01268j.
[10] N.A. Meredith, C. Quinn, D.M. Cate, T.H. Reilly, J. Volckens, C.S. Henry, Paper-based analytical devices for environmental analysis, Analyst 141 (2016) 1874–1887, https://doi.org/10.1039/c5an02572a.
[11] H.W. Gao, C.L. Yan, W. Wu, J. Li, Application of microfluidic chip technology in food safety sensing, Sensors 20 (2020), https://doi.org/10.3390/s20061792.
[12] L. Jiao, Q. Xu, J. Tong, S. Liu, Y. Hu, Q. Guo, H. Wu, W. Li, Q. Zhao, R. Chen, Facile preparation of pliable superamphiphobic papers with high and durable liquid repellency for anti-corrosion and open surface microfluidics, Appl. Surf. Sci. 606 (2022) 154845, https://doi.org/10.1016/j.apsusc.2022.154845.
[13] A. Alfadhel, J. Ouyang, C.G. Mahajan, F. Forouzandeh, D. Cormier, D. A. Borkholder, Inkjet printed polyethylene glycol as a fugitive ink for the fabrication of flexible microfluidic systems, Mater. Des. 150 (2018) 182–187, https://doi.org/10.1016/j.matdes.2018.04.013.
[14] Y. Temiz, R.D. Lovchik, G.V. Kaigala, E. Delamarche, Lab-on-a-chip devices: how to close and plug the lab? Microelectron. Eng. 132 (2015) 156–175, https://doi.org/10.1016/j.mee.2014.10.013.
[15] K. Giri, C.-W. Tsao, Recent advances in thermoplastic microfluidic bonding, Micromachines (basel) 13 (2022), https://doi.org/10.3390/mi13030486.
[16] Y. Luo, Z.B. Zhang, X.D. Wang, Y.S. Zheng, Ultrasonic bonding for thermoplastic microfluidic devices without energy director, Microelectron. Eng. 87 (2010) 2429–2436, https://doi.org/10.1016/j.mee.2010.04.020.
[17] Z. Zhang, X. Wang, Y. Luo, S. He, L. Wang, Thermal assisted ultrasonic bonding method for poly(methyl methacrylate) (PMMA) microfluidic devices, Talanta 81 (2010) 1331–1338, https://doi.org/10.1016/j.talanta.2010.02.031.
[18] S.P. Ng, F.E. Wiria, N.B. Tay, Low distortion solvent bonding of microfluidic chips, Procedia Eng. 141 (2016) 130–137, https://doi.org/10.1016/j.proeng.2015.09.212.
[19] J. Li, Z. Liu, R. Zhang, G. Luo, Y. Sun, J. Zhang, Q. Shen, Surface treatment and solvent co-assisted easy direct bonding of polymer/metal, Mater. Des. 204 (2021) 109641, https://doi.org/10.1016/j.matdes.2021.109641.
[20] B. Jiang, H. Guo, D. Chen, M. Zhou, Microscale investigation on the wettability and bonding mechanism of oxygen plasma-treated PDMS microfluidic chip, Appl. Surf. Sci. 574 (2022) 151704, https://doi.org/10.1016/j.apsusc.2021.151704.
[21] K. Liu, J.Z. Xiang, Z. Ai, S.K. Zhang, Y. Fang, T. Chen, Q.W. Zhou, S.Z. Li, S. X. Wang, N.G. Zhang, PMMA microfluidic chip fabrication using laser ablation and low temperature bonding with OCA film and LOCA, Microsyst. Technol. Micro Nanosyst. -Inf. Storage Process. Syst. 23 (2017) 1937–1942, https://doi.org/10.1007/s00542-016-2924-1.
[22] B. Zhao, D. Kontziampasis, L. Huang, W. Wu, B. Jiang, An innovative patternable microelectrode bonding technology for high-performance and cost-effective sealing in microfluidic chips, Chem. Eng. J. 503 (2025) 158214, https://doi.org/10.1016/j.cej.2024.158214.
[23] A. Welle, E. Gottwald, UV-based patterning of polymeric substrates for cell culture applications, Biomed. Microdevices 4 (2002) 33–41, https://doi.org/10.1023/A:1014267712144.
[24] C.-W. Tsao, D.L. DeVoe, Bonding of thermoplastic polymer microfluidics, Microfluid Nanofluidics 6 (2009) 1–16, https://doi.org/10.1007/s10404-008-0361-x.
[25] C. Chu, B. Jiang, L. Zhu, F. Jiang, A process analysis for microchannel deformation and bonding strength by in-mold bonding of microfluidic chips, J. Polym. Eng. 35 (2015) 267–275, https://doi.org/10.1515/polyeng-2013-0092.
[26] B. Zhao, W. Wu, M. Zhou, B. Jiang, G. Ziegmann, Highly dynamic tempered in-mold thermocompression bonding of microfluidic chips: process characteristics

and bonding performances, J. Mater. Res. Technol. 24 (2023) 639–652, https://doi.org/10.1016/j.jmrt.2023.03.040.
[27] B. Zhao, F. Mo, W. Wu, B. Jiang, G. Ziegmann, Deformation patterns and coordination mechanisms of cross-size microchannels during thermocompression bonding process, J. Mater. Res. Technol. 26 (2023) 3701–3709, https://doi.org/10.1016/j.jmrt.2023.08.141.
[28] X.Y. Chen, T.Y. Li, S. Zhang, Z. Yao, X.D. Chen, Y. Zheng, Y.L. Liu, Research on optimizing parameters of thermal bonding technique for PMMA microfluidic chip, Int. Polymer Process. J. Polymer Process. Soc. 32 (2017) 394–398.
[29] R. Sivakumar, N.Y. Lee, Microfluidic device fabrication mediated by surface chemical bonding, Analyst 145 (2020) 4096–4110, https://doi.org/10.1039/d0an00614a.
[30] C.L. Cassano, A.J. Simon, W. Liu, C. Fredrickson, Z.H. Fan, Use of vacuum bagging for fabricating thermoplastic microfluidic devices, Lab Chip 15 (2015) 62–66, https://doi.org/10.1039/c4lc00927d.
[31] H.Y. Zhang, F.Z. Fang, M.D. Gilchrist, N. Zhang, Precision replication of micro features using micro injection moulding: process simulation and validation, Mater. Des. 177 (2019), https://doi.org/10.1016/j.matdes.2019.107829.
[32] I.M. Gadala, M.A. Wahab, A. Alfantazi, Numerical simulations of soil physicochemistry and aeration influences on the external corrosion and cathodic protection design of buried pipeline steels, Mater. Des. 97 (2016) 287–299, https://doi.org/10.1016/j.matdes.2016.02.089.
[33] H.W. Wang, H.W. Zhou, H.W. Ji, X.C. Zhang, Application of extended finite element method in damage progress simulation of fiber reinforced composites, Mater. Des. 55 (2014) 191–196, https://doi.org/10.1016/j.matdes.2013.09.071.
[34] A. Borók, K. Laboda, A. Bonyár, PDMS bonding technologies for microfluidic applications: a review, Biosensors (basel) 11 (2021), https://doi.org/10.3390/bios11080292.
[35] C.L. Cassano, A.J. Simon, W. Liu, C. Fredrickson, Z. Hugh Fan, Use of vacuum bagging for fabricating thermoplastic microfluidic devices, Lab Chip 15 (2015) 62–66, https://doi.org/10.1039/c4lc00927d.
[36] M. Busek, S. Nøvik, A. Aizenshtadt, M. Amirola-Martinez, T. Combriat, S. Grünzner, S. Krauss, Thermoplastic elastomer (TPE)–poly(methyl methacrylate) (PMMA) hybrid devices for active pumping PDMS-free organ-on-a-chip systems, Biosensors (basel) 11 (2021), https://doi.org/10.3390/bios11050162.
[37] X. Ku, G. Zhuang, G. Li, A universal approach for irreversible bonding of rigid substrate-based microfluidic devices at room temperature, Microfluid Nanofluidics 22 (2018) 17, https://doi.org/10.1007/s10404-018-2039-3.
[38] H.D. Lynh, C. Pin-Chuan, Novel solvent bonding method for creation of a three-dimensional, non-planar, hybrid PLA/PMMA microfluidic chip, Sens Actuators A Phys 280 (2018) 350–358, https://doi.org/10.1016/j.sna.2018.08.002.
[39] M. Madadi, A. Madadi, R. Zareifar, A. Nikfarjam, A simple solvent-assisted method for thermal bonding of large-surface, multilayer PMMA microfluidic devices, Sens Actuators A Phys 349 (2023) 114077, https://doi.org/10.1016/j.sna.2022.114077.
[40] N. Ling, J.S. Lee, N.Y. Lee, Solvent-assisted low-temperature and low-pressure poly (methylmethacrylate) bonding coupled with selective microchannel hydrophobic coating for reliable sealing, Sens Actuators A Phys 265 (2017) 168–173, https://doi.org/10.1016/j.sna.2017.08.023.
[41] A. Bamshad, A. Nikfarjam, H. Khaleghi, A new simple and fast thermally-solvent assisted method to bond PMMA–PMMA in micro-fluidics devices, J. Micromech. Microeng. 26 (2016) 65017, https://doi.org/10.1088/0960-1317/26/6/065017.
[42] B. Zhao, W. Wu, B. Jiang, The in-mold thermocompression bonding process of microfluidic chips based on the highly dynamic variotherm technology: Process characteristics, in: NanoMan 2022 and AETS 2022 - 2022 8th International Conference on Nanomanufacturing and 4th AET Symposium on ACSM and Digital Manufacturing, 2022: pp. 1–6. https://doi.org/10.1109/Nanoman-AETS56035.2022.10119480.
[43] M. Shi, Y. Zhang, L. Cheng, Z. Jiao, W. Yang, J. Tan, Y. Ding, Interfacial diffusion and bonding in multilayer polymer films: a molecular dynamics simulation, J. Phys. Chem. B 120 (2016) 10018–10029, https://doi.org/10.1021/acs.jpcb.6b04471.
[44] M. Zhou, X. Xiong, D. Drummer, B. Jiang, Molecular dynamics simulation on the effect of bonding pressure on thermal bonding of polymer microfluidic chip, Polymers (basel) 11 (2019) 557, https://doi.org/10.3390/polym11030557.
[45] T. Ge, F. Pierce, D. Perahia, G.S. Grest, M.O. Robbins, Molecular dynamics simulations of polymer welding: strength from interfacial entanglements, Phys. Rev. Lett. 110 (2013) 98301, https://doi.org/10.1103/PhysRevLett.110.098301.